RSC Advances

PAPER

View Article Online
View Journal | View Issue

Cite this: *RSC Adv.*, 2015, **5**, 84988

Electrochemical and magnetic properties of nanostructured $CoMn_2O_4$ and Co_2MnO_4†

Neha Garg,[a] Monu Mishra,[b] Govind[b] and Ashok Kumar Ganguli*[ac]

In this study, we have focused on the synthesis of cobalt manganite nanostructures using a simplistic hydrothermal route. We have explored these spinels as alternative low-cost bifunctional electrocatalysts for oxygen reduction/evolution reactions (ORR/OER). Herein, we have developed energy-saving, facile and rapid synthetic methodologies for highly active spinel electrocatalysts. Two spinel phases, cubic Co_2MnO_4 and tetragonal $CoMn_2O_4$ have been successfully obtained by tuning the stoichiometric ratio of Co and Mn salts respectively. These $CoMn_2O_4$ and Co_2MnO_4 nanocubes have been used as bifunctional catalysts towards OER and ORR. Electrocatalytic experiments show that cubic Co_2MnO_4 nanocubes show five times higher activity towards ORR than tetragonal $CoMn_2O_4$ nanocubes while the tetragonal phase is a better electrocatalyst towards OER than the cubic Co_2MnO_4 phase. XPS studies revealed two types of oxygen (lattice O and surface adsorbed O species like OH^-) and the efficiency of the catalyst could be related to the binding affinity of oxygen. This explains the better catalytic activity of cubic Co_2MnO_4 which has a large percentage of adsorbed oxygen species. The stability of the catalyst was confirmed by carrying out TEM studies on a sample after carrying out 25 cycles. Magnetization experiments reveal that both the tetragonal $CoMn_2O_4$ as well as cubic Co_2MnO_4 show hysteresis at 10 K and 100 K without reaching saturation, which confirms an existing ferrimagnetic order in the samples. Both the tetragonal and cubic phases show $T_c \sim 110$ K and 150 K respectively.

Received 21st August 2015
Accepted 23rd September 2015

DOI: 10.1039/c5ra16937b

www.rsc.org/advances

Introduction

Spinel compounds or mixed transition-metal oxides (MTMOs) (denoted as $A_xB_{3-x}O_4$; A, B = Co, Ni, Zn, Mn, Fe *etc.* X = chalcogen) have attracted great research interest due to their wide applications in magnetism, electronics and catalysis, including electrochemical energy storage and conversion devices.[1–3] These mixed transition metal oxides consist of the combination of two simple low-cost transition metal oxides (TMOs), or a TMO and a post-TMO, into spinel-like structures ($A_xB_{3-x}O_4$) with stoichiometric or even non-stoichiometric compositions but can be obtained as a single-phase ternary metal oxide with two different metal cations. In the spinel type compounds AB_2O_4, A and B as divalent and trivalent metal ions respectively, occupy part or all of the tetrahedral and octahedral sites correspondingly and oxygen anions are arranged in a face centred cubic (fcc) lattice.[4,5] Among various spinels, MMn_2O_4 (M = Co, Mn, Cu, Ni *etc.*) is one of the most interesting mixed transition metal oxides in which one of the metal ion is manganese which has low cost, high abundance, low toxicity, multiple valence and shows a prominent Jahn–Teller effect.[6] Manganese-based spinels have numerous applications in lithium insertion electrodes, magnetism and catalysis.[7–9] Among all the manganites (MMn_2O_4), Co and Mn based spinel oxides ($Co_xMn_{3-x}O_4$) have been investigated extensively as promising electrode materials towards electrochemical energy and storage devices like in lithium ion batteries (LIBs), metal–O_2 batteries (MOBs, for example Zn–O_2 and Li–O_2 batteries), and fuel cells (FCs).[10–12] The complex chemical compositions of the MTMOs and their synergetic effects contribute to the high specific capacity/capacitance which results in exceptionally high electrochemical activity, than other electrode materials.[13] In the spinels, the presence of multiple valences of the cations (Co and Mn ions) helps to obtain the desirable electrochemical behaviour towards oxygen reduction reaction (ORR) for high-performance metal-O_2 batteries and fuel cells through multiple donor–acceptor chemisorption sites, responsible for the reversible adsorption of oxygen.[14,15] Ternary transition metal oxides show higher electrical conductivity than simple transition metal oxides due to the relatively low activation energy for electron transfer between cations.[16–18]

$Mn_xCo_{3-x}O_4$ $(0 \leq x \leq 3)$ is a good example of the relationship between solid state chemistry and electrocatalysis. From the

[a]*Department of Chemistry, Indian Institute of Technology, Hauz Khas, New Delhi 110016, India. E-mail: ashok@chemistry.iitd.ac.in*

[b]*Physics of Energy Harvesting, National Physical Laboratory (CSIR), New Delhi, 110012, India*

[c]*Institute of Nano Science and Technology, Mohali, Punjab 160062, India*

† Electronic supplementary information (ESI) available: Details of FTIR spectra of $CoMn_2O_4$ and Co_2MnO_4 nanostructures, TEM-EDX of (a) $CoMn_2O_4$ and (b) Co_2MnO_4 nanostructures, nitrogen adsorption and desorption isotherms measured at 77 K for (a) $CoMn_2O_4$ and (b) Co_2MnO_4. See DOI: 10.1039/c5ra16937b

earlier studies by Wickham and Croft[19] and Naka *et al.*,[20] it is confirmed that a single stable phase of the cubic spinel exists at 1000 °C only for $0 \leq x \leq 1.3$ while only tetragonal spinels exist for $x > 1.9$ and both the cubic and tetragonal spinels coexist in the range of $1.3 \leq x \leq 1.9$. It has been shown that the distribution of Co and Mn ions in $Co_{3-x}Mn_xO_4$ as $Co^{2+}[Co^{3+}{}_{2-x}Mn^{3+}{}_x]O_4$ with Curie temperature for $T_c = 191$ K ($x \sim 1.2$) while decreases with further increase in x.[19] In 1963, Blasse has reported that Co_2MnO_4 ($x = 1$) is inverse spinel with divalent cobalt and tetravalent manganese ions, $Co^{2+}[Co^{2+}Mn^{4+}]O_4$.[21] Lotgering *et al.*[22] have reported the ferrimagnetic behaviour of the cubic spinel Co_2MnO_4. Joy *et al.* have reported ferrimagnetic behaviour with $T_c \sim 183$ K.[23] The structural, magnetic and electronic properties of $Mn_xCo_{3-x}O_4$ have been reported over the whole range of x in the literature.[19,24] Since these compounds are extensively used in industry as thermistors, only the high-temperature resistivity studies have been reported.

The physicochemical properties of these mixed transition metal oxides are highly affected by their compositions, structures and oxidation state of metal ions, which depends on the synthesis procedure.[6,8] Traditional synthesis methods like solid state ceramic route involve high temperature and long heating time which will affect the electrochemical properties of the compounds.[25] Previously Co_2MnO_4 has been synthesized by solid state method at high temperature (1200 °C),[23] sol–gel process,[11] organic co-precipitation route,[26] flux method,[27] thermal decomposition of organometallic compounds[28] *etc.* But still rapid and rational synthesis of these manganites with controlled morphology at ambient condition is a challenge.

In our study, we have synthesized cobalt manganite nanostructures *via* a facile hydrothermal route without using any surfactant. We have stabilized both the cubic and tetragonal phases of $Mn_xCo_{3-x}O_4$ by tuning the reaction conditions. These cobalt manganite nanocubes have been used as bifunctional electrocatalyst towards oxygen reduction reaction (ORR) and oxygen evolution reaction (OER). Cubic Co_2MnO_4 phase shows higher electrocatalytic activity towards ORR than tetragonal $CoMn_2O_4$ while for the OER, catalytic activity is better for the tetragonal phase. We have also done the magnetic measurements for both the cubic and tetragonal phases and observed the saturation magnetization (M_s), coercivity (H_c) and remanent magnetization (M_r) of $CoMn_2O_4$ and Co_2MnO_4 nanocubes. At the low temperature ~10 K, saturation magnetization (M_s at 6 T) for Co_2MnO_4 is ten times higher than tetragonal $CoMn_2O_4$ phase.

Results and discussion

Herein, we have synthesized $CoMn_2O_4$ and Co_2MnO_4 phases through a simple one pot approach using hydrothermal method without using any surfactant or any controlling agent. The PXRD patterns from Fig. 1(a) shows the prominent diffraction peaks corresponding to the reflections from (101), (112), (200), (103), (211), (202), (220), (204), (312), (321), (224), (400), which could be indexed on the basis of tetragonal space group $I4_1/amd$ (no. 141) and concurred with the standard values of tetragonal $CoMn_2O_4$ (JCPDS card no. 77-471). No impurity peak was observed and the refined lattice parameters of body centered phase of tetragonal $CoMn_2O_4$ are $a = 5.784(6)$ Å, and $c = 9.091(2)$ Å. Similarly from Fig. 1(b), all the Bragg peaks (111), (220), (311), (222), (400), (422), (511), (440) were corresponding to the cubic structure of Co_2MnO_4 (space group of $Fd\bar{3}m$ with JCPDS card no. 840482). Pure face centred cubic phase of Co_2MnO_4 has been obtained without any impurity peak of the single metal oxide either cobalt oxide or manganese oxide. Refined lattice parameters for the cubic phase of Co_2MnO_4 was found to be $a = 8.290(4)$ Å which is slightly higher than previously reported.[15] Increase in the lattice cell parameters for $CoMn_2O_4$ as well as for Co_2MnO_4 confirms the nanocrystalline behaviour[29] of the particles obtained here.

The FTIR spectra Fig. S1 (ESI†) are very similar for both the samples and reveal a finger print of the Co–Mn spinel oxides. From the Fig. S1(a),† it is confirmed that the bands at around 630 cm^{-1} can be attributed to the vibration of the atoms in the tetrahedral oxygen environment (mainly cobalt, Co–O), while those around 525 cm^{-1} can be related to the vibration of the atoms in the octahedral oxygen environment (mainly manganese, Mn–O). These values are quite similar to the previous literature values known for cobalt manganites.[30] The broader peaks of $CoMn_2O_4$ compared to Co_2MnO_4 indicates that the tetragonal spinel contains a distribution of metal (Co & Mn) cations over the tetrahedral and octahedral sites.[31]

The morphology of the cobalt manganite nanostructures have been investigated using transmission electron microscopy (TEM). From the Fig. 2(a) and (b), The TEM images of the Co_2MnO_4 and $CoMn_2O_4$ products show well-defined cubic morphology. The enlarged TEM images reveals that the edge length of $CoMn_2O_4$ cubes is ~30–40 nm while for the Co_2MnO_4 nanocubes, edge length is ~20 nm.

High resolution TEM (HRTEM) image of Fig. 3(a) displays, distinct lattice fringes with an interplanar distance of 0.23 nm, corresponding to the reflection of (211) planes of $CoMn_2O_4$ crystals and the HRTEM image (Fig. 3(b)) show lattice spacing of 0.25 nm, resulting from (311) planes of tetragonal Co_2MnO_4.

Energy-dispersive X-ray spectrometry (EDS) mapping analysis (Fig. 4(a) and (b)) shows that the Co and Mn are uniformly distributed in $CoMn_2O_4$ as well as in Co_2MnO_4 nanocubes.

Furthermore, from the energy-dispersive spectrum (EDS), quantitative analysis has been done. Fig. S2(a) (ESI†) confirms the ratio of Co : Mn is 1 : 2 in $CoMn_2O_4$ while from Fig. S2(b) (ESI†), it is confirmed that Co : Mn ratio is 2 : 1 in Co_2MnO_4 nanostructures.

To obtain more detailed information about elemental composition and oxidation state of the $CoMn_2O_4$ and Co_2MnO_4 nanocubes, we have carried out the X-ray photoelectron spectroscopy (XPS) analysis. The survey scan (Fig. 5(a) and (b)) represents the presence of cobalt, manganese, oxygen and carbon in both the samples.

The presence of carbon and additional oxygen is associated with the impurities incorporated in the sample during sample mounting and loading. The Co $2P_{3/2}$ peak was deconvoluted into two major components at 779.4 eV and 780.5 eV which are attributed to +2 and +3 states respectively along with shakeup satellite (Fig. 6(a) and (c)).[32,33]

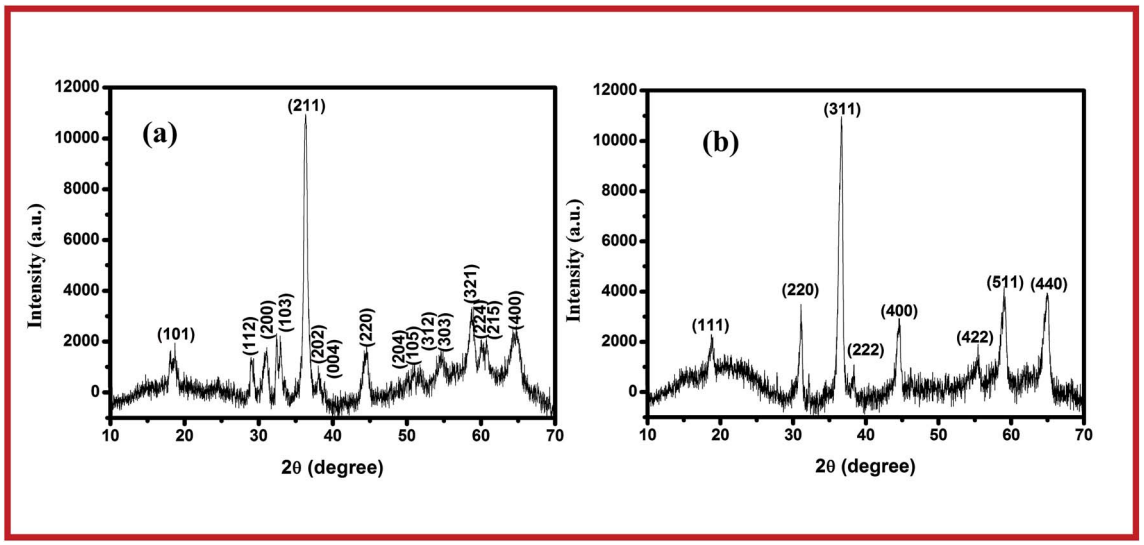

Fig. 1 Powder X-ray diffraction of (a) $CoMn_2O_4$ and (b) Co_2MnO_4 nanostructures.

The XPS results (Table 1) suggest that for the oxides ($Co_{3-x}Mn_x$ O_4), the Co^{2+}/Co^{3+} ratio increases with x[34] as Co^{2+} oxidation state dominates in $CoMn_2O_4$ while Co^{3+} state dominates in Co_2MnO_4. The deconvoluted Mn $2P_{3/2}$ core level depicts two identified peaks at 641.5 eV and 643.1 eV associated with +2 and +3 state.[35]

The specific surface area of cobalt-manganese oxide nanocubes were obtained by Brunauer–Emmett–Teller (BET) nitrogen adsorption/desorption measurements. The isothermal plots of N_2 adsorption/desorption for the Co_2MnO_4 and $CoMn_2O_4$ nanocubes with hysteresis loop between adsorption and desorption are shown in Fig. S3 (a) and (b) (ESI†). On the basis of the BET equation, the specific surface area of the $CoMn_2O_4$ and Co_2MnO_4 are ~35 m^2 g^{-1} and ~40 m^2 g^{-1}, respectively. The difference in surface area of the two nanostructures is not significant as the particle size and dimensions of the nanocubes in both the compounds like $CoMn_2O_4$ and Co_2MnO_4 is almost equal, as confirmed by TEM study.

Fig. 7 shows the zero-field-cooled (ZFC) and field cooled (FC) magnetization curves at 500 Oe. The magnetization during FC for both samples increase with decreasing temperature. The Curie temperature of ~110 K was found for $CoMn_2O_4$, which is almost equal to that reported by Zhang *et al.*[36]

From Fig. 7, it is confirmed that T_c for Co_2MnO_4 nanocubes is ~150 K which is lower than bulk Co_2MnO_4 (~183 K).[23] Thus as expected the T_c decreases with decreasing particle size. Magnetization with respect to magnetic field up to 7 T of $CoMn_2O_4$ and Co_2MnO_4 nanocubes was recorded at 200 K, 100 K and 10 K.

It can be noted from Fig. 8(a) and (b), the *M vs. H* curves of both $CoMn_2O_4$ and Co_2MnO_4 recorded at 10 K and 100 K show hysteresis without reaching saturation, which confirms an existing ferrimagnetic order in the present samples. The magnetization curve at 200 K is linear, which is consistent with the paramagnetic state as inferred from the *M* (T) curve (Fig. 7). The observed saturation magnetization (M_s), coercivity (H_c) and remanent magnetization (M_r) values of $CoMn_2O_4$ and Co_2MnO_4 nanocubes are given in Table 2.

Fig. 9 shows the ORR characteristics recorded on glassy carbon electrodes loaded with the $CoMn_2O_4$ and Co_2MnO_4

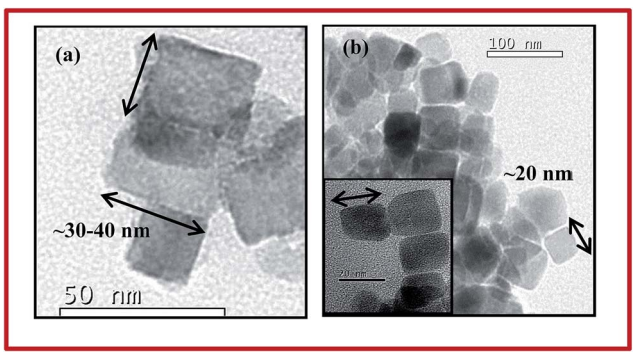

Fig. 2 Transmission electron micrographs of $CoMn_2O_4$ and Co_2MnO_4 nanostructures.

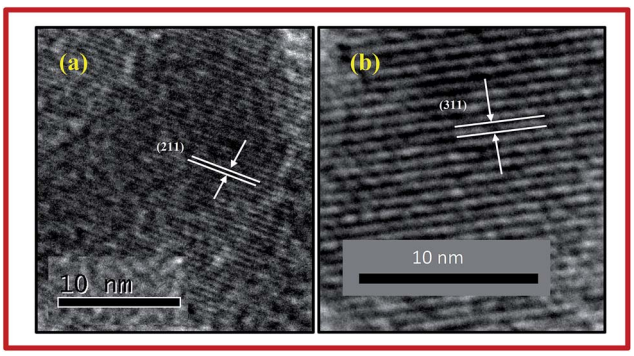

Fig. 3 HRTEM images of (a) $CoMn_2O_4$ and (b) Co_2MnO_4 nanostructures.

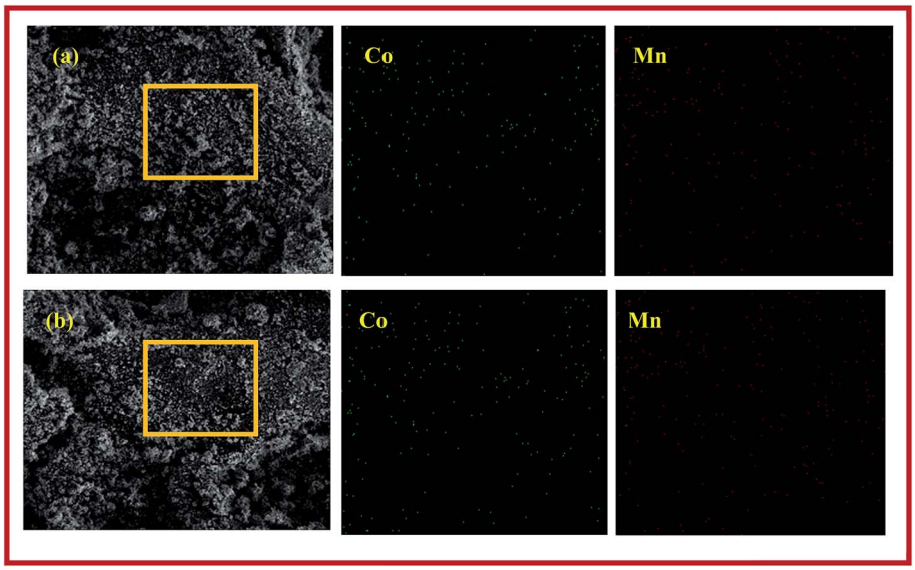

Fig. 4 Elemental EDX mapping of (a) $CoMn_2O_4$ and (b) Co_2MnO_4 nanostructures.

nanostructures. Fig. 9(a) shows the linear sweep voltammogram of the ORR, measured on rotating disk electrodes (RDEs) which exhibited similar profiles for both the Co–Mn oxide nanostructures, with two regions of potential–current response. It is confirmed that as the potential is scanned cathodically, the detected currents increase rapidly in the mixed kinetic–diffusion control region (approximately −0.1 to −0.45 V) and then in the presence of diffusion-limiting currents (I_d). The measured current decreases as observed for other nanostructured transition-metal oxides MnO_2, C-supported Mn oxides *etc.*[37,38] From the LSV (Linear Sweep Voltammetry), clearly the nanocrystalline cubic phase of Co_2MnO_4 outperformed the corresponding tetragonal phase in terms of having a higher positive onset potential and larger value of current. The ORR onset potential and peak potential of Co_2MnO_4 were −0.2 V and −0.45 V with current density of ∼2.5 mA cm^{-2} which is almost five times higher than that obtained for the tetragonal $CoMn_2O_4$ nanostructures (onset potential ∼ −0.28 V and peak potential ∼ −0.47 V with current density ∼ −0.5 mA cm^{-2}).

The electrocatalytic activity of Co_2MnO_4 towards ORR was analyzed by six sets of voltammetry curves which were recorded on RDEs at different speeds of rotation (400, 800, 1200, 1600, 2000 and 2400 rpm). Fig. 9(b) demonstrates that the current increased with rising rotational rates (ω) as a result of the faster oxygen flux to the electrode surface. Theoretically, the observed rotation speed (ω) dependent current (I) can be expressed by the Koutechky–Levich (K–L) eqn (1),[31,39] for analyzing ORR kinetics (Fig. 9(c)) by calculating the transferred electron number per oxygen molecule (n) during ORR.[32]

$$\frac{1}{J} = \frac{1}{J_L} + \frac{1}{J_K} = \frac{1}{B\omega^{\frac{1}{2}}} + \frac{1}{J_K} \quad (1)$$

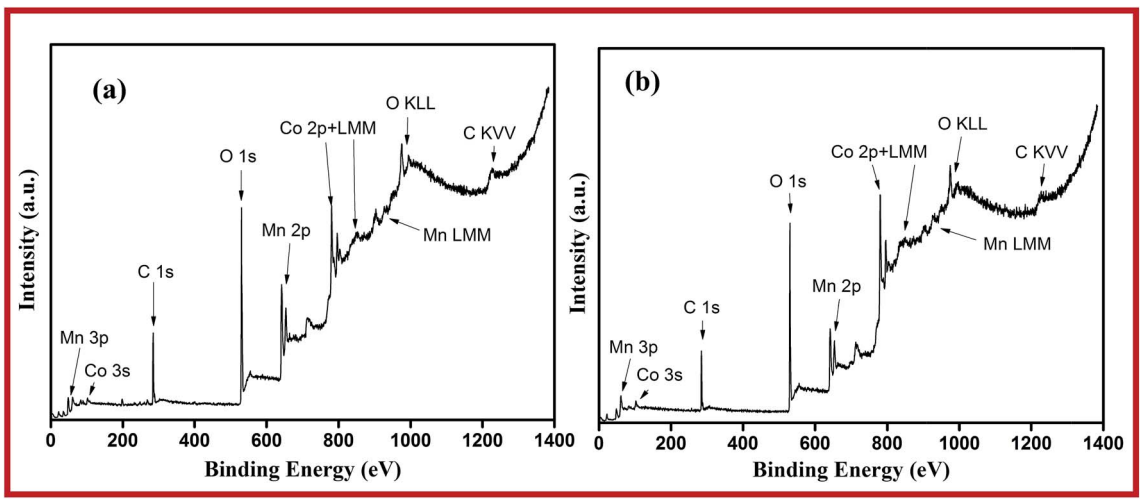

Fig. 5 Survey spectrums for both the (a) $CoMn_2O_4$ and (b) Co_2MnO_4 nanocubes.

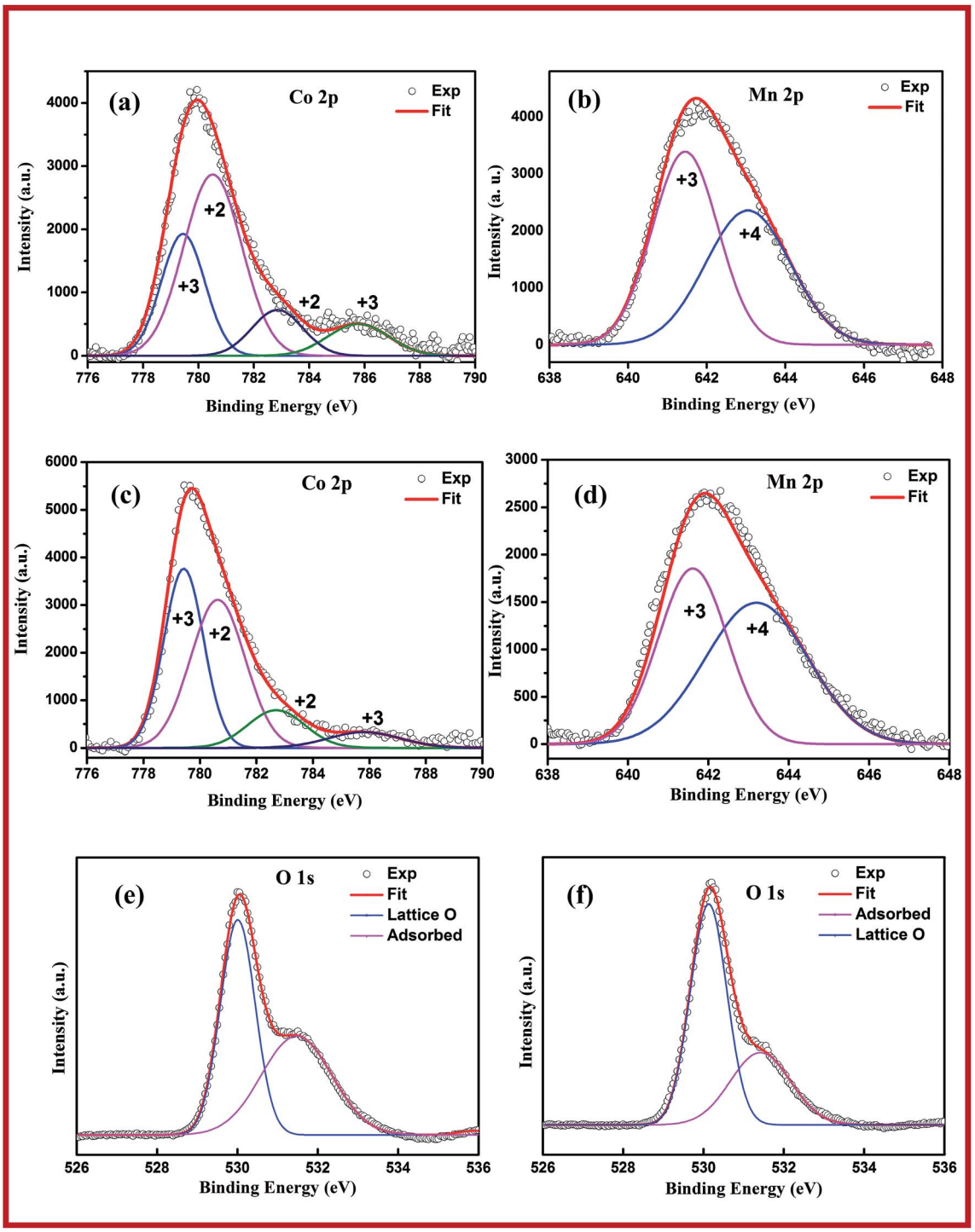

Fig. 6 XPS spectra of $CoMn_2O_4$ (a) Co2p core level, (b) Mn 2p core level, and (e) O 1s core level and of Co_2MnO_4 (c) Co 2p core level, (d) Mn 2p core level, and (f) O 1s core level respectively.

$$B = 0.62nFC_oD_o^{2/3}v^{-1/6} \quad (2)$$

$$J_K = nFkC_o \quad (3)$$

where J is the measured current density, J_K and J_L are the kinetic and diffusion-limiting current densities, ω is the angular velocity, n is transferred electron number, F is the Faraday constant, C_o is the bulk concentration of O_2, v is the kinematic viscosity of the electrolyte, and k is the electron-transfer rate constant.

Fig. 9(c) shows the constructed K–L curves, which plot I^{-1} *versus* $\omega^{-1/2}$ at −0.45 V, 0.4 V and −0.35 V, where the transferred electron number per oxygen molecule (n) in the ORR can be

Table 1 Percentage analysis of the Co and Mn ions in $CoMn_2O_4$ and Co_2MnO_4 nanostructures

Compounds	Co^{2+}	Co^{3+}	Mn^{3+}	Mn^{4+}
$CoMn_2O_4$	52.5	26.5	52.7	47.3
Co_2MnO_4	38.5	43.8	45.46	54.53

calculated from the slopes of the fitted linear line. For Co_2MnO_4, two approximate linear regions for each potential are seen, with the slopes changing from a value corresponding to $n \sim 3$ at the lower overpotential, as $2e^-$ process dominates over $4e^-$ process and lower rotation rates to a value for $n = 2$ for the higher overpotential and higher rotation rates.

These changes in the number of electrons of the Koutecky–Levich slopes were reported by Vago and Calvo *et al.*[40] for O_2 reduction on iron oxides. According to these results, it is proposed that the ORR based on Co_2MnO_4 electrocatalyst follows the 2-electron mechanism. The current was observed due to the catalytic oxygen reduction and the ORR mechanism of OH^- production on Co_2MnO_4 may be described by partial reduction with two step 2 electron process yielding HO_2^- ions as recorded for manganese oxide[41]

$$O_2 + H_2O + 2e^- \rightarrow HO_2^- + OH^-, \quad E^\circ = -0.065 \text{ V } \textit{vs.} \text{ NHE for pOH} = 0 \quad (4)$$

Followed by either the $2e^-$ reduction of HO_2^-

$$HO_2^- \text{ (ads)} + H_2O + 2e^- \rightarrow 3OH^-, \quad E^\circ = 0.867 \text{ V } \textit{vs.} \text{ NHE for pOH} = 0 \quad (5)$$

Or by the purely chemical disproportionation reaction of HO_2^- in solution

$$2HO_2^- \text{ (ads)} \rightarrow O_2 + 2OH^- \quad (6)$$

In agreement to previous studies,[42] at low rotation rates or low overpotential, this reaction may be followed by a slow disproportionation reaction of HO_2^- (eqn (6)), and when HO_2^- is completely disproportionate, it involves overall 4^- electron process per O_2 molecule.[43] The prevalence of the $2e^-$ process at high overpotential can be attributed to the fact that under this condition the oxidation reaction of the HO_2^- ion (eqn (6)) goes in backward direction. Hence, the overall process of ORR involving four electrons may occur at a large extent near the equilibrium potential for the HO_2^- reduction step as follows

$$O_2 + 2H_2O + 4e^- \rightarrow 4OH^-, \quad E^\circ = 0.401 \text{ V } \textit{vs.} \text{ NHE for pOH} = 0 \quad (7)$$

For the nanocrystalline Co_2MnO_4 spinels, the steady currents observed in the continuous polarization period of 6000 s (Fig. 9(d)), indicates the stability of the catalyst in an alkaline

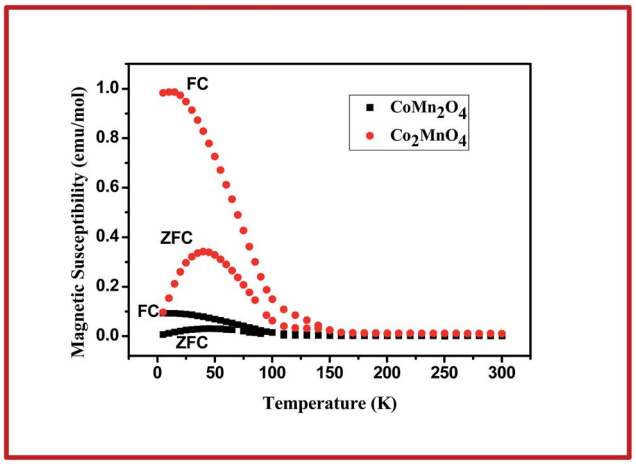

Fig. 7 The temperature dependence of magnetization at applied field of 500 Oe.

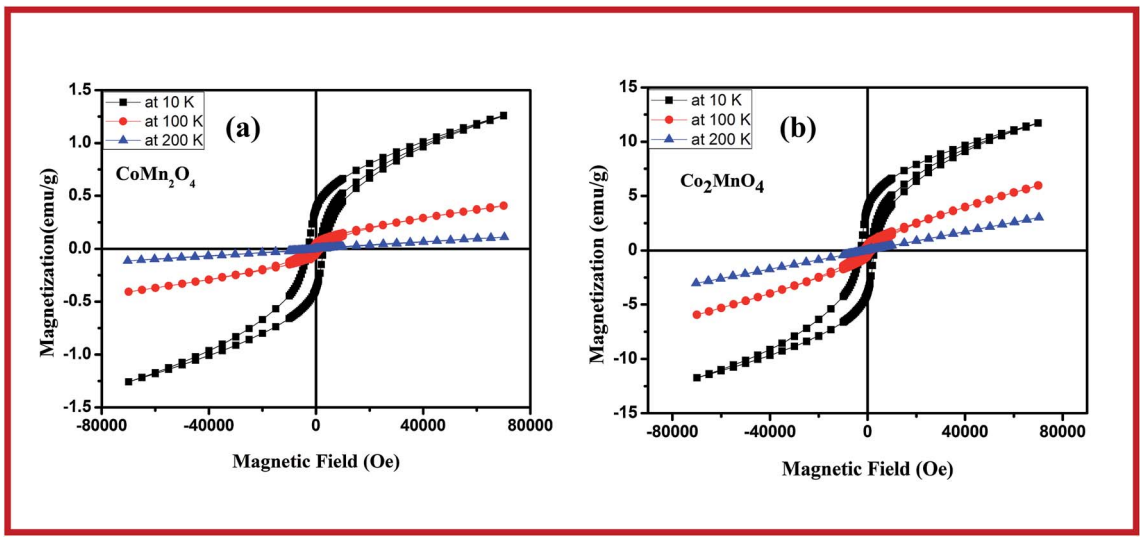

Fig. 8 *M vs. H* plot of (a) $CoMn_2O_4$ and (b) Co_2MnO_4 nanocubes at 7 T.

Table 2 Details of the magnetic properties of $CoMn_2O_4$ and Co_2MnO_4 nanostructures

Sample	Temperature (K)	Saturation magnetization (M_s at 6 T) (emu g^{-1})	Remanent magnetization (M_r) (emu g^{-1})	Coercive field (H_c) (Oe)
$CoMn_2O_4$	10 K	1.18	0.37	2846
	100 K	0.37	0.05	1722
	200 K	Paramagnetic behavior		
Co_2MnO_4	10 K	11	3.9	2750
	100 K	5.3	0.5	1810
	200 K	Paramagnetic behavior		

medium. Also in the inset of Fig. 9(d), TEM image of Co_2MnO_4 taken after the electrocatalytic measurements shows that there is no variation in the morphology of the Co_2MnO_4 nanocubes, which confirms the morphological stability of Co_2MnO_4 catalyst. The good ORR stability of the Co_2MnO_4 nanocubes could be attributed to the structural and chemical stability of the spinel phase in the alkaline medium.[44] The ORR performance of the Co_2MnO_4 nanocubes (regarding to onset potential and current density) was compared with the carbon-supported platinum nanoparticles (Pt/C),[15] which is nearly comparable. The relatively lower onset potential for the spinels could be improved by cation doping or metal decorating to change the surface electronic properties or enhance conductivity.[45] Thus, it is clear that nanocrystalline cobalt manganite spinels (Co_2MnO_4 nanocubes) should find a practical application in metal–air batteries and fuel cell applications.

Mixed transition metal oxide based spinel structures have been shown to be a good water oxidation catalyst for oxygen evolution reaction.[46] In our study we have explored the cobalt manganites as a bifunctional catalyst towards electrochemical reactions (both ORR and OER). So, in our next step, we have measured the catalytic behavior of $CoMn_2O_4$ and Co_2MnO_4

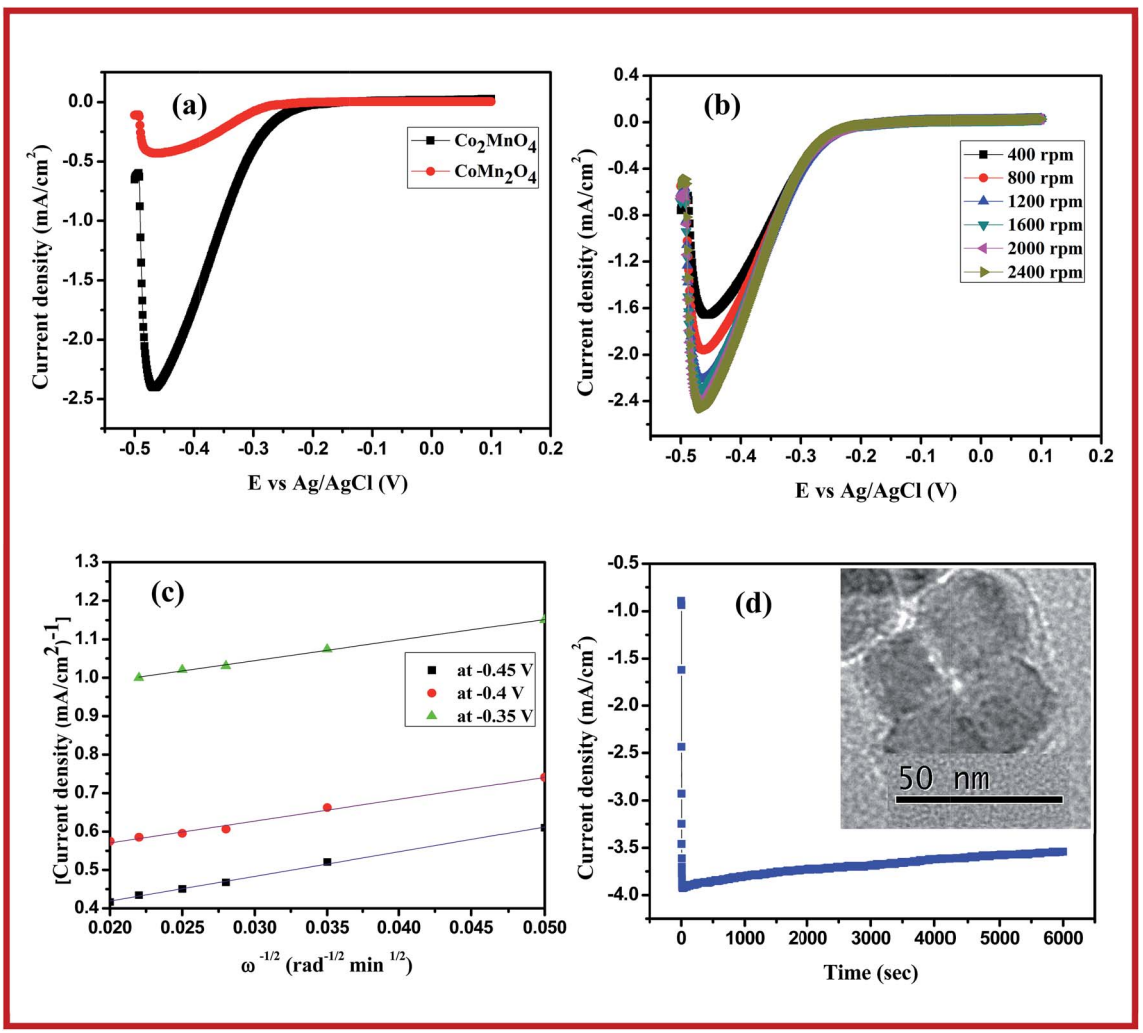

Fig. 9 Electrochemical application of nanocrystalline $CoMn_2O_4$ and Co_2MnO_4 as ORR electrocatalyst (a) linear sweep voltammogram (LSV) of the ORR using catalyst-modified RDEs in O_2-saturated alkaline electrolyte at 400 rpm (b) rotation-speed dependent current–potential curves recorded on Co_2MnO_4 electrodes in O_2-saturated 1 M KOH solution and (c) the corresponding K–L curve (d) chronoamperometry curves of the ORR for Co_2MnO_4 nanocubes obtained at −0.45 V in oxygen-saturated 0.1 M KOH under constant rotating (400 rpm).

using cyclic voltammetry in 1 M KOH in the potential range of 0.0–1.0 V (Fig. 10(a)). It is evident that the tetragonal $CoMn_2O_4$ nanostructures exhibited higher activity than the corresponding cubic Co_2MnO_4 phase. $CoMn_2O_4$ nanocubes generate an OER current nearly five times higher than that of the Co_2MnO_4 nanocubes, which is in contrast with the results for ORR. The tetragonal phase ($CoMn_2O_4$) shows the current density of ~45 mA cm^{-2} (at 1 V) and overpotential of ~0.38 V while on the other hand, for cubic Co_2MnO_4, the current density and overpotential was observed to be ~8 mA cm^{-2} and ~0.4 V respectively (Fig. 10(a)).

Stability of an electrode is also one of the main factors which affect their usability in electrochemical applications.[47] The studies on $CoMn_2O_4$ nanostructures (Fig. 10(b)) for 25 consecutive cycles show negligible variation in activity indicating its stability in alkaline medium. We have also done the TEM analysis of $CoMn_2O_4$ after the electrocatalytic experiments towards OER and we have observed the nanocrystalline morphology of $CoMn_2O_4$ nanocubes which describes the morphological stability of the catalyst. From the above results, it is confirmed that among both the phases, catalytic activity of cubic Co_2MnO_4 is higher than tetragonal $CoMn_2O_4$ towards ORR while for OER, the reactivity order is reverse as tetragonal $CoMn_2O_4$ > cubic Co_2MnO_4. Since the catalytic process for oxygen reduction involves the reduction and oxidation of surface metal oxide species, the number and activity of these redox centres would be important factors to define the catalytic performance, also ORR activity is associated with the absorption affinity for oxygen.[48–50] To explain the differences in the intrinsic activities of the cubic (Co_2MnO_4) and tetragonal ($CoMn_2O_4$) spinels, we have performed X-ray photoelectron spectroscopy (XPS) (Fig. 6). Compositional analysis of the elements and the percentage of the oxidation states of both the Co and Mn elements are given in Table 1. From the above results it is confirmed that in $CoMn_2O_4$, Co(II) dominates over Co(III) and Mn(III) dominates over Mn(IV), while in the cubic Co_2MnO_4, we have observed that Co(III) extent is higher than Co(II) and also Mn(IV) is higher than Mn(III). From the Table 1, it is confirmed that the relative intensity and percentage of Mn(IV) is higher in cubic spinel (Co_2MnO_4) rather than in tetragonal phase $CoMn_2O_4$.

Oxidation state dependent electrocatalytic activity of the transition metal oxides towards ORR reaction is attributed to the following sequence of reactions, which involves the change of Mn(IV) to Mn(III) and involves overall 2-electron 2-step process during ORR:[51]

$$Mn^{4+} + e^- \rightarrow Mn^{3+} \text{ (fast)} \quad (8)$$

$$O_2 \rightarrow O_{2,ads} \text{ (fast)} \quad (9)$$

$$Mn^{3+} + O_{2,ads} \rightarrow Mn^{4+} + O_{2,ads}^- \text{ (slow)} \quad (10)$$

$$O_{2,ads}^- + H_2O + e^- \rightarrow HO_{2,ads}^- + OH^- \text{ (fast)} \quad (11)$$

where the rate determining step (eqn (10)) is related to the electron transfer of Mn(III) to the adsorbed oxygen without O_2 splitting. At low rotation rates and low overpotential, this reaction sequence is followed by the disproportionation of HO_2^- (Reaction (6)), recycling O_2 and, eventually leading to the participation of $4e^-$ per O_2 molecule. The large reactivity of Co_2MnO_4 with higher extent of Mn(IV) was ascribed to the occurrence of a mediation processes (according to eqn (8)) involving the reduction of Mn(IV) to Mn(III), followed by the electron transfer of Mn(III) to oxygen. Koutecky–Levich analyses have shown that the electrode reaction goes though the 2-electron mechanism to produce HO_2^- followed by a disproportion reaction of HO_2^- into O_2 and OH^-.[43] Higher activity of cubic phase towards ORR is also described by stronger oxygen binding ability of Co_2MnO_4 than the tetragonal phase $CoMn_2O_4$.

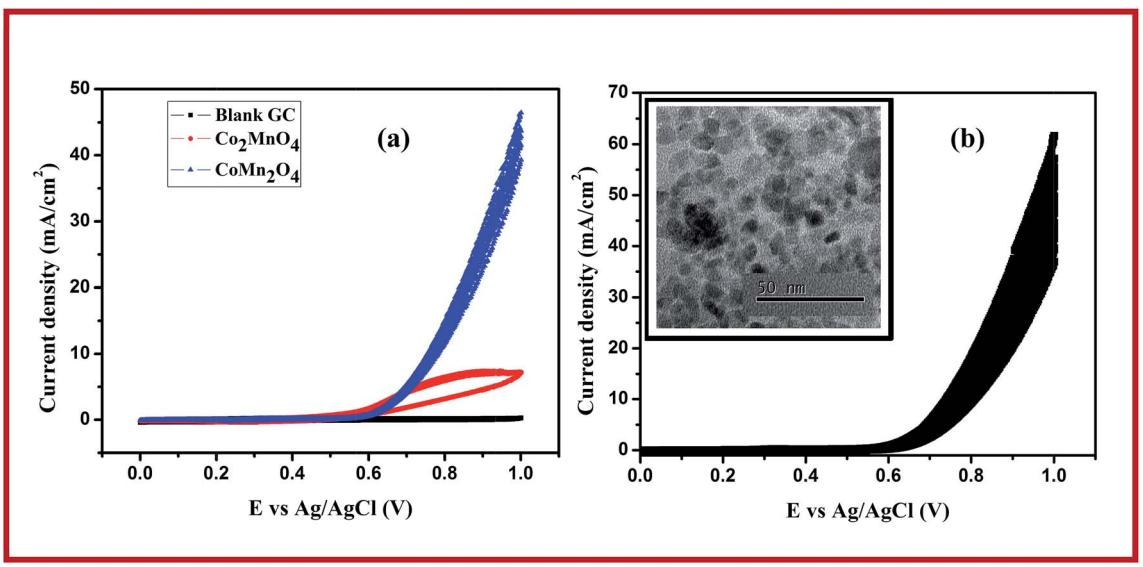

Fig. 10 (a) Cyclic voltammogram of the OER in 1 M KOH electrolyte (b) stability curve of $CoMn_2O_4$ nanostructures for 25 cycles.

Table 3 Percentage calculation of adsorbed oxygen in $CoMn_2O_4$ and Co_2MnO_4 nanostructures

Sample peak position	Lattice O	Adsorbed O
$CoMn_2O_4$ (530.2)	530.1 (65%)	531.4 (35%)
Co_2MnO_4 (530.0)	530.0 (52%)	531.4 (48%)

Fig. 8(e) and (f) shows the asymmetric O 1 s signal can be deconvoluted into two distinguishable peaks centred at 530.0 and 531.4 eV, which correspond to lattice oxygen and surface adsorbed oxygen-containing species (possibly hydroxide or water).[36,52] The multistep process of electrocatalytic oxygen reduction involves the formation of HO_2^- species followed by its further decomposition/reduction to OH^- ions.[15] The whole electrocatalytic oxygen reduction process is dependent on available active sites on catalyst surface and the absorption affinity of oxygen.[46,48,53] The relative intensity and peak areas corresponding to the adsorbed oxygen species (OH^-) in deconvoluted O (1s) Fig. 8(e) and (f) spectra was observed to be higher for the cubic spinel phase. This specifies a stronger oxygen affinity for the cubic phase compared to tetragonal spinel phase. Note that the relative intensity and peak areas corresponding to the adsorbed oxygen species are higher for the cubic spinel than for the tetragonal spinel, which indicates the stronger oxygen affinity of the cubic phase (Table 3).

Theoretical calculations (DFT) of binding energies (E_b) of an oxygen molecule on Co/Mn defect sites show that cubic surface generates much more stable molecular oxygen adducts than the tetragonal surface.[15] Furthermore, the surfaces of both phases (cubic as well as tetragonal) contain moreover the same value of surface area or the same number of catalytic sites per surface unit cell, whereas the area of the cubic Co_2MnO_4 unit cell is smaller. Therefore, for a given surface area, the number of available active sites of the cubic Co_2MnO_4 surface surpasses that on the tetragonal $CoMn_2O_4$ surface. All these factors are responsible for the enhanced ORR catalytic activity of cubic spinel nanocubes of $CoMn_2O_4$.

Experimental details

Materials and methods

$Co(CH_3COO)_2\cdot 4H_2O$ (CDH, 99%), $Mn(CH_3COO)_2\cdot 4H_2O$ (CDH, 99%), NH_4OH (Fisher Scientific, 25% NH_3), ethanol (Merck, 96%) and KOH (Fisher Scientific, 85%) were used in the synthesis of $CoMn_2O_4$ and Co_2MnO_4 nanostructures.

Synthesis of $CoMn_2O_4$ and Co_2MnO_4 nanostructures. All the chemical reagents were of analytical grade and used without further purification. In a typical synthesis of $CoMn_2O_4$, mixture of $Co(CH_3COO)_2\cdot 4H_2O$ (0.1 M), $Mn(CH_3COO)_2\cdot 4H_2O$ (0.1 M) (Co : Mn: 1 : 2), and NH_4OH (0.1 M) were loaded into a 100 mL Teflon-lined autoclave. After 1 h of magnetic stirring, the autoclave was sealed and maintained at 180 °C for 24 h and then allowed to cool at room temperature. The product was collected by centrifugation, washed several times with absolute ethanol and distilled water, and finally dried at room temperature.

For the synthesis of Co_2MnO_4, only the ratio of $Co(CH_3COO)_2\cdot 4H_2O$ (0.1 M) and $Mn(CH_3COO)_2\cdot 4H_2O$ (0.05 M) is different (Co : Mn: 2 : 1) otherwise all the other conditions for the preparation of Co_2MnO_4 is kept same as for the synthesis of $CoMn_2O_4$ nanostructures.

Characterization

Powder X-ray diffraction data was collected using a Bruker D8 Advance diffractometer with Ni-filtered Cu Kα radiation (λ = 1.5418 Å) source. For the X-ray measurements, 2-theta range was set from 10° to 70° at a scanning speed of 0.02° s^{-1} while tube voltage and current were fixed at 40 kV and 30 mA respectively. Raw data were exposed to background correction and Kα_2 lines were removed. Refinement of the lattice parameters of the observed '*d*' values was done by least squares fit of the observed *d*-values using Powder Cell software.[54] FTIR studies of $CoMn_2O_4$ and Co_2MnO_4 nanostructures were carried out on a Nicolet Protege 460 spectrometer with KBr disk in the range of 500–4000 cm^{-1}. Structure and composition investigation of the $CoMn_2O_4$ and Co_2MnO_4 nanostructures were carried out by transmission electron microscopy (TEM) and energy dispersive X-ray analysis (EDX) studies on a FEI Technai G^2 20 electron microscope operated at 200 kV. TEM specimens were prepared by dispersing the sample in ethanol by ultrasonic treatment and pouring a drop of the dispersion on a porous carbon film supported copper grid which was then dried in air at room temperature. To investigate the homogeneity and distribution of the metal ions in both the $CoMn_2O_4$ and Co_2MnO_4, elemental EDX mapping has been done using FESEM-EDX (FESEM, JEOL and JSM-6700 F). X-ray photoelectron spectroscopy measurements have been carried out in ultrahigh vacuum based Omicron Multiprobe Surface Analysis System operating at a base pressure of 5×10^{-11} Torr. For XPS analysis, monochromatic Al-K$_\alpha$ radiation source (1486.7 eV) was employed. An OMICRON EA125 hemispherical analyser (operating at pass energy of 20 eV) equipped with a 7 channeltron parallel detection unit was used to collect the XPS spectra. The calibration of binding energy in photoemission spectra was done referring to Au $4f_{7/2}$ emission line.[55] The core level (CL) fitting has been done using Shirley background and Voigt line shape after necessary carbon correction.

Nitrogen adsorption–desorption isotherms were recorded at liquid nitrogen temperature (77 K) using a Nova 2000e (Quantachrome Corp.) equipment and the specific area was determined by the Brunauer–Emmett–Teller (BET) method. The samples were degassed at 150 °C for 4 h prior to the surface area measurements. Temperature dependent magnetization was carried out with a SQUID (*superconducting quantum interference device*) under field-cooled (FC) and zero-field-cooled (ZFC) conditions in the temperature range of 5–300 K in presence of an applied magnetic field of 500 Oe. Magnetic hysteresis measurements have been carried out at 10 K, 100 K and 200 K up to 7 T. Electrocatalytic experiments were performed with a computer-controlled electrochemical work-station (Metrohm Autolab 302/PGSTAT). The three-electrode cell consists of reference electrode as Ag/AgCl, Pt wire as counter electrode and glassy carbon as working electrode. Glassy carbon electrode

(GCE) was polished using (0.05 μm) alumina paste, ultrasonication treatment was done in distilled water and in ethanol for the electrocatalytic studies (both oxygen evolution reaction (OER) as well as oxygen reduction reaction (ORR)).

Fabrication of the electrode for electrocatalysis measurement

A mixture of 5 mg of the catalyst with 5 μl of isopropyl alcohol was prepared by ultrasonication for 30 min and 5 μl of Nafion was added as a binder. From the above solution, 2 drops were taken and placed on the glassy carbon electrode and air-dried for 1 h. 1 M KOH was used as an electrolyte and the glassy carbon electrode was placed in the cell containing 40 mL of 1 M KOH solution. For each experiment freshly prepared solutions of KOH was used. Cyclic voltammetry (CV) experiment was carried out at room temperature with a scan rate of 0.01 V s^{-1} with a peak window between 0 and 0.9 V *vs.* Ag/AgCl electrode. All potentials were referred to the reference electrode. All electrochemical measurements were performed at 25 °C.

Rotating disk electrode (RDE) measurement

The catalyst modified working electrode was prepared by the same method as for CV. The working electrode was scanned cathodically at a rate of 5 mV s^{-1} with varying rotating speed from 400 to 2400 rpm. Koutecky–Levich plots (J^{-1} *vs.* $\omega^{-1/2}$) were analysed at various electrode potentials. The slopes of their best linear fit lines were used to calculate the number of electrons transferred (n) on the basis of the Koutecky–Levich equation.[56]

Conclusions

Nanocrystalline $Mn_xCo_{3-x}O_4$ spinels with $x = 1$ (Co_2MnO_4) and $x = 2$ ($CoMn_2O_4$) have been synthesized as bifunctional catalysts *via* a facile hydrothermal route. Two distinct pure phases (cubic and tetragonal) of cobalt manganites have been obtained by tuning the reaction parameters and the stoichiometric ratio of Co and Mn. The cubic phase Co_2MnO_4 outperforms the tetragonal phase towards ORR activity while the tetragonal phase ($CoMn_2O_4$) shows five times higher activity towards OER than the cubic spinel (Co_2MnO_4). The intrinsic electrocatalytic activity of cubic and tetragonal Co–Mn–O spinels correlates with the oxygen binding ability on the catalyst surface. The presence of larger amount of Mn(IV) and larger binding affinity for oxygen enhances the activity of Co_2MnO_4 towards ORR. These results reveal that mixed transition metal manganites possess long-term stability under anodic conditions, good electrical conductivity and high electrocatalytic performances towards oxygen evolution reaction as well as towards oxygen reduction reaction that may be of significant applications in metal–air batteries and fuel cells.

Acknowledgements

A. K. G. thanks CSIR, DST and DIT Government of India for financial support. NG is thankful to UGC, Government of India for fellowship. We thank Dr Kanaga Raj for their prolific discussions regarding magnetic experiments.

References

1 J. Hemberger, P. Lunkenheimer, R. Fichtl, H. A. Krug von Nidda, V. Tsurkan and A. Loidl, *Nature*, 2005, **434**, 364.
2 H. J. Fan, M. Knez, P. Scholz, K. Nielsch, E. Pippel, D. Hesse, M. Zacharias and U. Gösele, *Nat. Mater.*, 2006, **5**, 627.
3 M. Matsuda, H. Ueda, A. Kikkawa, Y. Tanaka, K. Katsumata, Y. Narumi, T. Inami, Y. Ueda and S. H. Lee, *Nat. Phys.*, 2008, **3**, 397.
4 M. A. Willard, Y. Nakamura, D. E. Laughlin and M. E. McHenry, *J. Am. Ceram. Soc.*, 1999, **82**, 3342.
5 W. H. Bragg, *Nature*, 1915, **95**, 561.
6 D. P. Shoemaker, J. Li and R. Seshadri, *J. Am. Chem. Soc.*, 2009, **131**, 11450.
7 M. M. Thackeray, *Prog. Solid State Chem.*, 1997, **25**, 1.
8 H. C. Choi, J. H. Shim and B. I. Min, *Phys. Rev. B: Condens. Matter Mater. Phys.*, 2006, **74**, 172103.
9 G. Fierro, G. Ferraris, R. Dragone, M. L. Jacono and M. Faticanti, *Catal. Today*, 2006, **116**, 38.
10 G. Zhang, L. Yu, H. B. Wu, H. E. Hoster and X. W. Lou, *Adv. Mater.*, 2012, **24**, 4609.
11 P. Lavela, J. L. Tirado and C. Vidal-Abarca, *Electrochim. Acta*, 2007, **52**, 7986.
12 J. Li, S. Xiong, X. Li and Y. Qian, *Nanoscale*, 2013, **5**, 2045.
13 M. Hamdani, R. N. Singh and P. Chartier, *Int. J. Electrochem. Sci.*, 2010, **5**, 556.
14 Y. Liang, H. Wang, J. Zhou, Y. Li, J. Wang, T. Regier and H. Dai, *J. Am. Chem. Soc.*, 2012, **134**, 3517.
15 F. Cheng, J. Shen, B. Peng, Y. Pan, Z. Tao and J. Chen, *Nat. Chem.*, 2011, **3**, 79.
16 T. Y. Wei, C. H. Chen, H. C. Chien, S. Y. Lu and C. C. Hu, *Adv. Mater.*, 2010, **22**, 347.
17 L. Hu, L. Wu, M. Liao, X. Hu and X. Fang, *Adv. Funct. Mater.*, 2012, **22**, 998.
18 S. Trasatti, *Electrodes of conductive metallic oxides Part A*, Elsevier Scientific Pub. Co., 1980, p. 227.
19 D. G. Wickham and W. J. Croft, *J. Phys. Chem. Solids*, 1958, **7**, 351.
20 S. Naka, M. Inagaki and T. J. Tanaka, *Mater. Sci.*, 1972, **7**, 441.
21 G. Blasse, *Philips Res. Rep.*, 1963, **18**, 38.
22 F. K. Lotgering, *Philips Res. Rep.*, 1956, **11**, 337.
23 P. A. Joy and S. K. Date, *J. Magn. Magn. Mater.*, 2000, **218**, 229.
24 I. Aoki, *J. Phys. Soc. Jpn.*, 1962, **17**, 53.
25 A. Stein, S. W. Keller and T. E. Mallouk, *Science*, 1993, **259**, 1558.
26 R. M. Rojas, E. Vila, O. Garcia and J. L. Martin de Vidales, *J. Mater. Chem.*, 1994, **4**, 1635.
27 Y. Matsushita, H. Ueda and Y. Ueda, *Nat. Mater.*, 2005, **4**, 845.
28 Y. Xu, X. Wang, C. An, Y. Wang, L. Jiao and H. Yuan, *J. Mater. Chem. A*, 2014, **2**, 16480.
29 F. Zhang, S. W. Chan, J. E. Spanier, E. Apak, Q. Jin, R. D. Robinson and I. P. Herman, *Appl. Phys. Lett.*, 2002, **80**, 127.
30 A. V. Salker and S. M. Gurav, *J. Mater. Sci.*, 2000, **35**, 4713.

31 S. A. Hosseini, D. Salari, A. Niaei, F. Deganello, G. Pantaleo and P. Hojati, *J. Environ. Sci. Health, Part A: Toxic/Hazard. Subst. Environ. Eng.*, 2011, **46**, 291.
32 A. Thissen, D. Ensling, F. J. F. Madrigal and W. Jaegermann, *Chem. Mater.*, 2005, **17**, 5202.
33 J. G. Kim, D. L. Pugmire, D. Battaglia and M. A. Langell, *Appl. Surf. Sci.*, 2000, **165**, 70.
34 A. Restovic, E. Ríos, S. Barbato, J. Ortiz and J. L. Gautier, *J. Electroanal. Chem.*, 2002, **522**, 141.
35 F. Chaochao, L. Guangshe, L. Dong, H. Xinsong, J. Zheng and L. Li, *ACS Appl. Mater. Interfaces*, 2014, **6**, 2439.
36 H. T. Zhang and X. H. Chen, *Nanotechnology*, 2006, **17**, 1384.
37 M. S. El-Deab and T. Ohsaka, *Angew. Chem., Int. Ed.*, 2006, **45**, 5963.
38 I. Roche, E. Chaînet, M. Chatenet and J. Vondrák, *J. Phys. Chem. C*, 2007, **111**, 1434.
39 A. J. Bard and L. R. Faulkner, *Electrochemical Methods Fundamentals and Applications*, Wiley, New York, 2001.
40 E. R. Vago and E. J. Calvo, *J. Electroanal. Chem.*, 1995, **388**, 161.
41 F. Cheng, Y. Su, J. Liang, Z. Tao and J. Chen, *Chem. Mater.*, 2010, **22**, 898.
42 L. Mao, D. Zhang, T. Sotomura, K. Nakatsu, N. Koshiba and T. Ohaka, *Electrochim. Acta*, 2003, **48**, 1015.
43 F. H. B. Lima, M. L. Calegaro and E. A. Ticianelli, *J. Electroanal. Chem.*, 2006, **590**, 152.
44 R. G. Cao, J. S. Lee, M. L. Liu and J. Cho, *Adv. Energy Mater.*, 2012, **2**, 816.
45 V. R. Stamenkovic, B. S. Mun, M. Arenz, K. J. J. Mayrhofer, C. A. Lucas, G. Wang, P. N. Ross and N. M. Markovic, *Nat. Mater.*, 2007, **6**, 241.
46 K. Kinoshita, *Electrochemical Oxygen Technology*, Wiley, 1992.
47 H. Zheng, J. Huang, W. Wang and C. Ma, *Electrochem. Commun.*, 2005, **7**, 1045.
48 J. Greeley, I. E. L. Stephens, A. S. Bondarenko, T. P. Johansson, H. A. Hansen, T. F. Jaramillo, J. Rossmeisl, I. Chorkendorff and J. K. Nørskov, *Nat. Chem.*, 2009, **1**, 552.
49 E. Ríos, S. Abarca, P. Daccarett, H. N. Cong, D. Martel, J. F. Marco, J. R. Gancedo and J. L. Gautier, *Int. J. Hydrogen Energy*, 2008, **33**, 4945.
50 P. Zoltowski, D. M. Drazic and L. Vorkapic, *J. Appl. Electrochem.*, 1973, **3**, 271.
51 J. P. Brenet, *J. Power Sources*, 1979, **4**, 183.
52 B. J. Tan, K. J. Klabunde and M. A. Sherwood, *J. Am. Chem. Soc.*, 1991, **113**, 855.
53 P. Strasser, S. Koh, T. Anniyev, J. Greeley, K. More, C. Yu, Z. Liu, S. Kaya, D. Nordlund, H. Ogasawara, M. F. Toney and A. Nilsson, *Nat. Chem.*, 2010, **2**, 454.
54 W. Kraus and G. Nolze, *Power Cell for Windows, Version 2.4*, Berlin, Germany, 2000.
55 S. K. Hong, T. Hanada, H. Makino, Y. Chen, H. JuKo, T. Yao, A. Tanaka, H. Sasaki and S. Sato, *Appl. Phys. Lett.*, 2001, **78**, 3349.
56 K. Yamamoto, T. Imaoka, W. J. Chun, O. Enoki, H. Katoh, M. Takenaga and A. Sonoi, *Nat. Chem.*, 2009, **1**, 397.